



TiO₂ mesocrystal with nitrogen and fluorine codoping during topochemical transformation: Efficient visible light induced photocatalyst with the codopants

Peng Zhang, Mamoru Fujitsuka, Tetsuro Majima*

The Institute of Scientific and Industrial Research (SANKEN), Osaka University, Mihogaoka 8-1, Ibaraki, Osaka 567-0047, Japan



ARTICLE INFO

Article history:

Received 28 October 2015

Received in revised form

29 November 2015

Accepted 11 December 2015

Available online 15 December 2015

Keywords:

Topochemical transformation

TiO₂ mesocrystal

Nitrogen and fluorine codoping

Visible light Photocatalyst

Charge transfer dynamics

ABSTRACT

TiO₂ mesocrystal (TMC) with {001} facet exposed is uniformly codoped with nitrogen (N) and fluorine (F) to form the TMC with N and F codoping (NFT) during the topochemical transformation. The visible light induced reduction of Cr(VI) to Cr(III) was evaluated with a clear correlation to their optical absorption due to the N dopant with the localized midgap state. The comparison of methylene blue (MB) degradation under the visible or UV light irradiation indicates that the F codoping with the role of water dissociation, is discerned to associate with N doping based on the comparison between NFT and NFT-NaOH with the treatment of NFT by NaOH aqueous solution for removing F. The unambiguously effect of surface adsorbed F as the assistant role of N in the localized midgap state is further elucidated from monitoring of charge separation and trapping processes using the femtosecond time-resolved diffused reflectance (TDR) measurement.

© 2015 Elsevier B.V. All rights reserved.

1. Introduction

The visible light induced photocatalyst has been widely progressed with continuous consideration on environmental pollution and insufficient natural energy. The photoactivation of TiO₂ has caused enormous interest to scientists and engineers after the photocatalytic water splitting reported by Fujishima and Honda in 1972 [1]. Due to the versatile physicochemical properties of nontoxicity, high chemical stability, low cost, and easy synthesis, TiO₂ is a promising photocatalyst to be applied in the wide range of solar-to-chemical energy conversion such as environmental remediation, solar water splitting, CO₂ photoreduction, and photovoltaic cells [2–5]. However, because of the intrinsic wide band gap, TiO₂ can be only excited under the UV light irradiation which covers less than ~5% of the solar spectrum. Aimed at the practical utilization of visible light, a variety of modifications are undertaken to tune the band gap of the electronic structure [6,7]. Among the metal and

non-metal doping, the N doping is the most efficient avenues to create N 2p in the localized midgap state leading to the increase of thermal stability and the decrease of recombination centers [8–10]. With the respect to synthesize N-doped TiO₂, a large amount of nitrification processes, such as wet and dry process with additional N source, are embodied in nano powders, thin films, nanotubes and nanowires [8–10]. However, it is still highly required a facile synthetic craft to dope N on anatase TiO₂ without the instrument-dependent and cost-ineffective treatment.

It is worthily mentioned that the large-scale preparation in practical application, the novel pyrolysis of Ti-compound containing dopants is proposed as the ideal candidate to acquire efficient doping [11]. The ammonium oxofluorotitanate is a fundamental group of Ti-compound for the synthesis of doped TiO₂ [12]. It is inferred that the anisotropic dissolution of NH₄TiOF₃ can chemically convert to TiO₂ mesocrystal (TMC) during the topochemical transformation, accompanying with N and F releasing [13–16]. As a new class of porous building blocks oriented assembly of nanocrystals, the obtained TMC with a well-defined crystal shape significantly enhances the charge separation with remarkably long-lived charges and exhibits excellent photocatalytic activities

* Corresponding author. Fax: +81 6 6879 8499.

E-mail address: majima@sanken.osaka-u.ac.jp (T. Majima).

compared with TiO_2 nanocrystals and commercial P25 [17–20]. It is a great of significance to introduce the dopant simultaneously from the original precursors or intermedium during the synthesis, without affecting the nucleation and growth of TMC. With more positive promotion of N doping for larger photostability and photocatalytic efficiency, it is an imperative issue to exploit the effects of the F codoping on the N-doped TMC with the visible light activity [6,21]. Although fascinating performances emerged in a variety of codoping methods have been studied, the mechanism of the interaction among versatile dopants is still inconclusive due to the complexity of the methods.

To resolve the scientific challenge in doping field, we report a novel strategy for the synthesis of TMC with the uniform distribution of N, F dopants from the direct annealing of the intermediate NH_4TiOF_3 during the topochemical transformation. The photoreductive efficiency of Cr(VI) to Cr(III) was correlated to the optical absorption dependent on the dopant content at various annealing temperatures. We confirmed the doping of N in the localized midgap state together with the surface adsorbed F enhanced the photocatalytic degradation of MB based on charge transfer dynamics under the visible or UV light irradiation. With the effect in promoting the visible light absorption and facilitating the degradation efficiency, the N and F codoping on TiO_2 as the prevalent photocatalyst will open a new road in the practical application under the solar light irradiation.

2. Experimental

2.1. Materials

The titanium(IV) fluoride was purchased from Sigma–Aldrich. The ammonium nitrate, ammonium fluoride, and boric acid were purchased from Wako Pure Chemical Industries. All of these chemicals were analytical grade and used as received.

2.2. Preparation of NH_4TiOF_3

The samples were synthesized with some modifications according to the previous reports [22–24]. A precursor solution containing TiF_4 , H_2O , NH_4NO_3 , and NH_4F (molar ratio = 1:503.4:4.9:2.4) was prepared, and were placed on a silicon wafer to form a thin layer. It was calcined in air using a heating rate of $10^\circ\text{C min}^{-1}$ at 160°C for 2 h. The annealed sample was collected for the further treatment.

2.3. Preparation of TiO_2 mesocrystal (TMC)

The as-prepared NH_4TiOF_3 was mixed with boric acid (0.5 M) at 60°C for 4 h and dried after washing by water and ethanol separately [25]. Furthermore, the obtained samples were calcined at 500°C for 0.5 h, which was referred as pristine TMC.

2.4. Preparation of doped TMC

The as-prepared NH_4TiOF_3 placed in a narrow neck vessel ($L \times R = 7.5 \text{ cm} \times 1.75 \text{ cm}$) with a lid was annealed in air with a heating rate of $20^\circ\text{C min}^{-1}$ at different temperatures for 0.5 h. The obtained samples were designed as NFT- x , in which the x represents the annealing temperatures. As a controllable reference, the NFT samples were treated with NaOH aqueous solution (0.01 M) in the dark for 8 h to remove the excess fluorine impurity, which was referred as NFT–NaOH [26].

2.5. Characterization

The structures of the samples were examined using X-ray diffraction (XRD; Rigaku, Smartlab; operated at 40 kV and 200 mA,

Cu $K\alpha$ source). The morphologies were investigated using field-emission scanning electron microscopy (FESEM) equipped with EDX analyzer (JEOL, JSM-6330FT) and transmission electron microscopy (TEM) equipped with EDX analyzer (JEOL, JEM-2100 operated at 200 kV). Scanning TEM (STEM) and energy dispersive spectroscopy (EDS) mapping were performed using a Cs corrected JEM-ARM200F microscope operated at 200 kV. The Brunauer–Emmett–Teller (BET) surface areas were measured using nitrogen sorption (BEL Japan, BELSORP max). The pore volumes and pore diameter distributions were derived from the adsorption isotherms using the Barrett–Joyner–Halenda (BJH) model. The steady state UV–vis absorption and diffuse reflectance spectra (DRS) were measured by UV–vis–NIR spectrophotometers (Shimadzu, UV-3100 or Jasco, V-570) at room temperature. The thermal analysis was performed by thermogravimetric analysis (Rigaku, Thermo plus EVO II/TG–DTA, TG8120) in N_2 . The X-ray photoelectron spectroscopy (XPS) spectral measurements were performed with the PHI X-tool (ULVAC-PHI). The total organic carbon (TOC) measurements were carried out by TOC analyzer (Shimadzu, TOC-VCSH).

2.6. Photocatalytic test

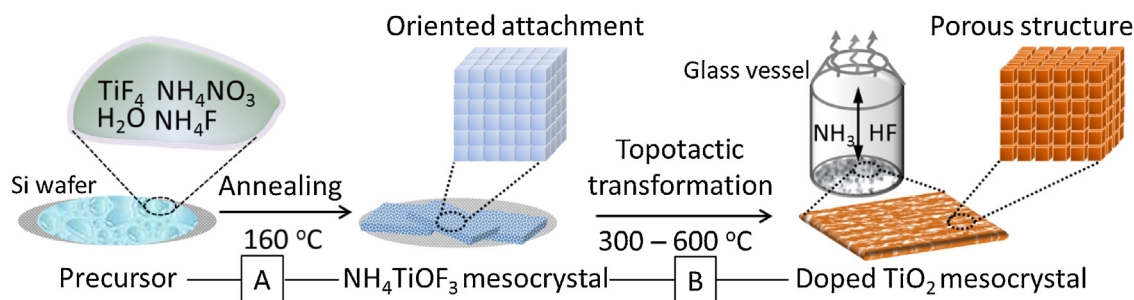
For a typical photocatalytic process, the catalytic dispersions (2 g L^{-1}) containing $\text{K}_2\text{Cr}_2\text{O}_7$ (Wako Pure Chemical Industries, 0.05 mM, pH 3) or methylene blue (Wako Pure Chemical Industries, 0.03 mM) were transferred to a quartz cuvette after sonication. The photocatalytic reaction was initiated by irradiation with UV-LED source (POT-365; 100 mW cm^{-2}) or Xenon lamp (HAL-320; 200 mW cm^{-2}), with constant magnetic stirring at room temperature. After stopping the light illumination, the sample was centrifuged at 10000 rpm (Hitachi, himac CF16RX) to separate the solid particles. The concentration of unreacted molecules, from which the degradation yield was calculated, was analyzed using a UV-visible-near infrared spectrophotometer (Shimadzu, UV-3600) at the characteristic wavelength. The apparent quantum efficiency (AQE) at each centered wavelength of the monochromatic light (Asahi Spectra, HAL-320; 0.7 mW cm^{-2}) was calculated from the ratio of the number of decomposed MBs to those of the irradiated photons by using the following expression: $\text{AQE} = (\text{number of decomposed MBs} / \text{number of incident photons}) \times 100\%$.

2.7. Time-resolved diffuse reflectance spectral measurements

The femtosecond diffuse reflectance spectra (TDR) were measured by the pump and probe method using a regeneratively amplified titanium sapphire laser (Spectra-Physics, Spitfire Pro F, 1 kHz) pumped by a Nd:YLF laser (Spectra-Physics, Empower 15). The seed pulse was generated by a titanium sapphire laser (Spectra-Physics, Mai Tai VFSJW; fwhm 80 fs). The fourth harmonic generation (330 or 440 nm, $3 \mu\text{J pulse}^{-1}$) of the optical parametric amplifier (Spectra-Physics, OPA-800CF-1) was used as the excitation pulse. A white light continuum pulse, which was generated by focusing the residual of the fundamental light on a sapphire crystal after the computer controlled optical delay, was divided into two parts and used as the probe and reference lights, of which the latter was used to compensate the laser fluctuation. Both the probe and reference lights were directed to the sample powder coated on the glass substrate, and the reflected lights were detected by a linear InGaAs array detector equipped with the polychromator (Solar, MS3504). The pump pulse was chopped by the mechanical chopper synchronized to one-half of the laser repetition rate, resulting in a pair of spectra with and without the pump, from which the absorption change (% Abs) induced by the pump pulse was estimated. All measurements were carried out at room temperature.

Table 1Structural characteristics of NH_4TiOF_3 , pristine TMC, and doped TMC at various annealing temperatures.

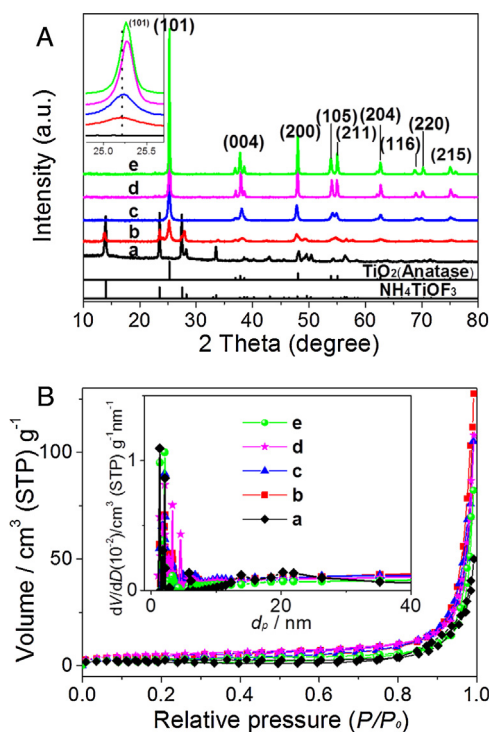
Sample	Surface area, $[\text{m}^2 \text{g}^{-1}]$	Pore volume, $[\text{cm}^3 \text{g}^{-1}]$	Pore size, $[\text{nm}]$	N content (wt%)	F content (wt%)
Pristine TMC	23	0.10	2.03	0.01	0.03
NH_4TiOF_3	7.4	0.03	1.34	14.20	33.16
NFT-300	16.0	0.07	2.06	5.43	20.4
NFT-400	16.1	0.07	2.07	2.30	6.1
NFT-500	17.7	0.06	2.08	3.23	4.87
NFT-600	9.79	0.05	2.08	3.03	3.78

**Fig. 1.** Schematic illustration of preparation for N and F doped TiO_2 mesocrystal (NFT).

3. Results and discussion

3.1. Synthesis and structures of doped TMC

To investigate the growth mechanism during the topochemical transformation (Fig. 1), the phase identification and the structural analysis of doped TMCs were performed from XRD, N_2 adsorption–desorption isotherm with pore size distribution, and the FESEM. After the water evaporation from the precursor (Process A), the phase of NH_4TiOF_3 was firstly formed on silicon wafer at 160 °C. The sheet-like NH_4TiOF_3 mesocrystal showed invisible pore superstructure on the surface (Fig. S1) and low surface area ($7.4 \text{ m}^2 \text{g}^{-1}$, Table 1) due to the assemble fusion [14,15]. Subsequently, the NH_4TiOF_3 mesocrystal was collected from silicon wafer and annealed in a narrow neck vessel to 200 °C (Process B). In this process, a portion of the intermediate NH_4TiOF_3 was converted to anatase TiO_2 (Fig. S2). It is noted that a major part of the NH_4TiOF_3 was transformed to anatase TiO_2 after calcined at 300 °C (Fig. 2A). Additionally, the surface structure started to decompose and merge to be the larger particles than NH_4TiOF_3 (Figs. 2 B and 3 A) [11]. Upon further annealing to 400 °C, the pure phase of anatase TiO_2 formed from NH_4TiOF_3 without morphology change, which is attributed to the topochemical transformation (Fig. 3B) [22]. More importantly during this process, the sources of N and F were released from the crystal lattice of NH_4TiOF_3 and doped on TMC simultaneously in a narrow neck vessel [25]. It reveals that the narrow neck vessel played a major contribution to confine the released gas spreading inside, instead of flow out immediately, and provide a saturated gas atmosphere for doping. The clear shrinks of the crystal lattice resulted from the doping are in good agreement with the movement of (1 0 1) diffraction peak toward to the higher angle range (Fig. 2A inset) [21–28]. When the annealing temperatures increased to 500 °C, the void was formed to create the visual porous structures between the adjacent nanocrystals (Fig. 3C). This result is consistent with decreasing gradually the specific surface area ($17.7 \text{ m}^2 \text{g}^{-1}$, Table 1) and increasing the particle size (2.08 nm, Table 1) due to the fusion of TiO_2 nanoparticles [22]. Continuously elevating up to 600 °C, most of the structures are collapsed inevitably into nanoscale particles (2.08 nm, Table 1) with the decrease of the surface area ($9.8 \text{ m}^2 \text{g}^{-1}$, Table 1) in Fig. 3D. But there was no remarkable impurity phase observed after the annealing at 600 °C due to its good thermal stability of the anatase phase

**Fig. 2.** (A) Powder XRD patterns with an enlarged (1 0 1) diffraction peak (inset), (B) N_2 adsorption–desorption isotherms and pore size distribution (inset) of (a) NH_4TiOF_3 , (b) NFT-300, (c) NFT-400, (d) NFT-500, and (e) NFT-600.

[22]. It can be deduced that the TMC undergoes crystal growth during the doping process, correlated to the strengthened crystallinity from the sharper diffraction peaks as the elevating temperatures. The series of annealed samples were referred as NFT- x , in which x represents the annealing temperature. As compared to the doped TMC, the pristine TMC showed a smaller average size, due to the dissolution and disaggregation during the recrystallization by the H_3BO_3 treatment (Table 1, Fig. S3) [11].

The morphology of NFT-500 was characterized by TEM in Fig. 4A. It is observed that NFT-500 has a sheet-like structure with {0 0 1} facet dominated from the selective area electron diffraction (SAED) in Fig. 4A inset [19]. Comparable to other samples with different

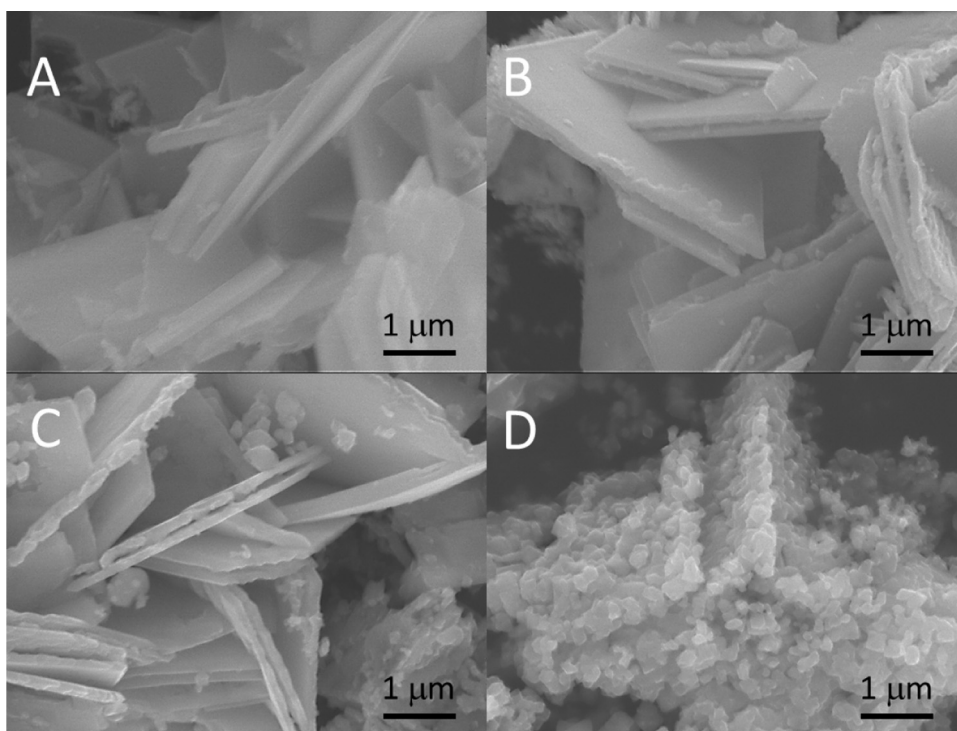


Fig. 3. FESEM images of (A) NFT-300, (B) NFT-400, (C) NFT-500, and (D) NFT-600.

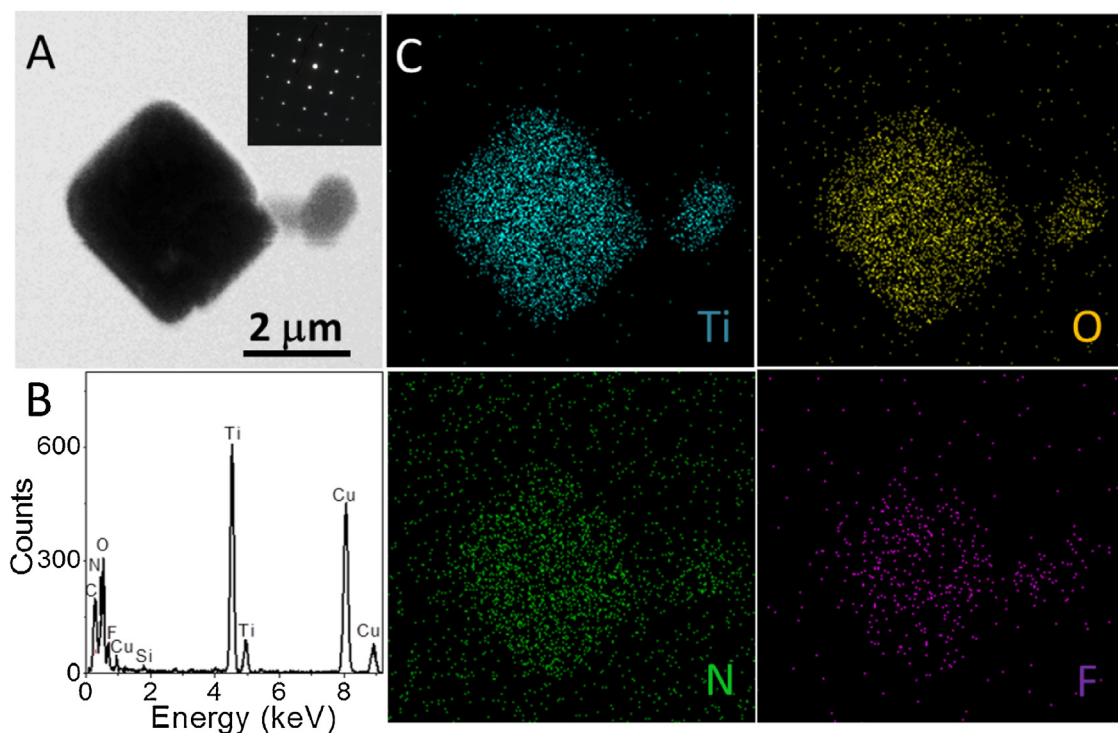


Fig. 4. (A) STEM, (B) EDX spectrum, and (C) elemental mapping images of NFT-500. The elements of Ti, O, N, and F are shown in blue, yellow, green, and purple color. (For interpretation of the references to color in this figure legend, the reader is referred to the web version of this article.)

annealing temperatures in Table 1, the EDS analysis of NFT-500 exhibited the high concentrations of N (3.23 wt%) and F (4.87 wt%) in Fig. 4B, showing that the N and F doping are strongly dependent on the elevating temperature [29,30]. From the elemental mapping in Fig. 4C, it is clearly observed that both N and F are doped on TMC superstructure with homogeneous distribution. The doping

intensity increased as the elevating temperature, which is in good agreement with the optical spectrum (see below). Their chemical composition of NFT-500 was analyzed by XPS (Fig. S4). The XPS spectra of F1s with binding energy around 684 eV and 688.5 eV are ascribed to the F absorbed on surface and substitution [28–31]. It has been reported that the substitutional N modification is formed

due to the detected N1s peak centered at 399 eV [9–32]. The well chemical distributions of the F and N were clearly observed from the XPS depth profile (Fig. S5). It revealed the atomic concentration of F and N showed the constant tendency after Ar⁺ etching from surface to a depth of several nanometers. Ti⁴⁺ on the surface was observed with two peaks of Ti 2p_{1/2} (465 eV) and Ti 2p_{3/2} (458 eV). In the O1s region, a clear peak around 532 eV assigned to the surface adsorbed–OH was observed together with other peak at 520 eV assigned to the lattice oxygen. On the other hand, the peaks of N 1s and F 1s with high-noise level were observed due to the low content of two dopants, which are consistent with the EDS results [31,32].

The optical responses of NFT are variable with the calcination temperature, which is indicated by the UV–vis diffuse reflectance spectra (DRS) in Fig. 5A. Compared with the pristine TMC, the absorption edge shifted to longer wavelength in the visible light region with increasing the calcination temperature [11]. It is remarkably worth that add-on shoulders were imposed from 380 nm to 550 nm due to the N doping with an isolated N 2 p state in the midgap. Because of F doping has no visible light responding [9], the absorption intensity in the visible region was determinant on the amount of N doped in the TMC. The absorption intensity of NFT-300 with higher content of N (5.43 wt%) was a bit enhanced due to the N component were mostly from the residue of NH₄TiOF₃ after annealing. In particular, for the NFT-400 with 2.3 wt% N doping, a new absorption band at a wavelength greater than 500 nm was observed. The effective extension for light absorption of NFT-500 was mainly response to the higher content of N dopants (3.23 wt%) dependent on the annealing temperature. Additionally, NFT-600 exhibited small decreasing in optical intensity due to the loss of two dopants (N, 3.03%; F, 3.78%) after the high temperature annealing (Table 1) [30]. It can be seen obviously the absorption edge are gradually red shift along with the annealing temperatures due to the tailed band formation after F codoped with N. With increasing the calcination temperature, the thermal conversion was monitored by the thermogravimetric analyses (TG–DTA) of NH₄TiOF₃ in Fig. 5B. After NH₄TiOF₃ was formed Eq. (1), there was no obvious weight loss below 200 °C where water is adsorbed on hygroscopic TiO₂ [14,15]. In the temperature range of 250 °C–500 °C, a sharp endothermic peak was arisen due to the chemical phase transformation from the intermedium to TiO₂ Eqs. (2) and (3). This implies that the major contributions of the weight loss are attributed to the progressive release of NH₃ and HF. In the closed glass vessel, it can be inferred that the amount of N and F was saturated firstly and then start to be doped on TMC gradually. Coincided with the result of XRD, there was also no additional weight loss observed from 500 °C to 600 °C during the topochemical transformation due to its good thermal stability with maximum doping [22,16,33].



3.2. Photocatalytic degradation on doped TMC

The photocatalytic reductive efficiency of pristine TMC and NFT synthesized at various temperatures was evaluated from the reduction of Cr(VI) to Cr(III) under the visible irradiation ($\lambda \geq 420$ nm, 200 mW cm⁻²) in Fig. 6. The reductive rate for Cr(VI) to Cr(III) was estimated to be 0.0011, 0.0013, 0.0017, 0.0066, and 0.0030 min⁻¹ for pristine TMC and NFT-300 ~ 600, respectively from the slopes of the linear plot between $\ln(C_0/C)$ and irradiation time. As compared to pristine TMC with feeble response to visible light, N and F doped TMC, NFT-300 and NFT-400, showed markedly improvement of the reductive efficiency due to the strengthen doping with the elevating

temperature. It was obviously shown that the NFT-500 with optimal ratio of NH₄NO₃ to NH₄F exhibited the highest photocatalytic efficiency due to the strongest ability of the visible light harvesting by the large amount of N doped content [34]. However, the NFT-500 with different ratio of NH₄NO₃ to NH₄F showed much lower activity, which is assigned to their disorder structures (Figs. S6 and S7) [22]. On the other hand, NFT-600 with similar optical response to NFT-500 showed nearly half efficiency, which were resulted from the poor charge migration among the random nanoparticles because of the collapsed mesocrystal structure [23,35]. The negligible degradation was observed in the absence of NFT or visible light irradiation. It is reasonable that the N content corresponds to the absorption ability from N in the localized midgap state, influencing the efficiency of the photoreduction of Cr(VI).

To clarify the role of F codoping on the predominant energy state of N, the NFT-500 was subsequently washed by NaOH aqueous solution (NFT–NaOH) to controllably remove the surface adsorbed F. The fraction of surface adsorbed –OH (532 eV) may be increased by removing F in a part (Table S1 and Fig. S4). Intriguingly, a die-off (20%) in Cr(VI) reduction by NFT–NaOH was observed even it possess the similar optical absorption and surface area to NFT-500 (Fig. S8 and Table S1). In order to clarify the interaction or effect of two dopants on the photocatalytic efficiency, the degradation of methylene blue (MB) was examined under the visible ($\lambda = 420 \sim 440$ nm, 200 mW cm⁻²) or UV light ($\lambda = 365$ nm, 100 mW cm⁻²) irradiation (Fig. 6B) [32]. The adsorption equilibrium of MB on NFT with different annealing temperatures was performed in the dark (Fig. S9). After the comparison of MB adsorption properties between the NFT-500 and others, it was found their surface area were strongly dependent on MB adsorbed abilities. Their photocatalytic degradation showed a clear linear ship to the adsorption properties of MB, which indicated the important factor of adsorption property in photocatalytic reaction. During the visible light irradiation, NFT-500 exhibited the highest degradation efficiency than the pristine TMC and NFT–NaOH, while no degradation was shown using the sole F doping TiO₂ under the visible light irradiation, because the atomic *p* level of F (*ca.* –11.0 eV) exists below the O (*ca.* –8.5 eV) and no visible absorption exists for the sole F doping TiO₂ [9]. The photocatalytic mineralization of MB was monitored via total organic carbon (TOC) in Fig. 6C. The NFT-500 showed a larger rate constant of TOC disappearance (0.19 min⁻¹) than the pristine TMC (0.05 min⁻¹), indicating a clear correlation of MB converted to harmless gaseous CO₂ and inorganic ions. It was found that the MB can be completely decolorized and effectively mineralized with an average overall TOC removal to 70% after 1 h, which revealed a similar tendency to the result from UV–vis spectrometry. On contrary, the pristine TMC with intrinsic absorption showed the superior efficiency under the UV irradiation in spite of the negligible activity under the visible light irradiation. The duplicated runs were carried out to average the results with the similar tendency. It is suggested that the poor contribution of surface adsorbed F for NFT–NaOH is leading to the lower photocatalytic efficiency under the visible or UV light case [30]. From the comparison of the redox reaction under the visible or UV light irradiation, it is indicated that the effect of N and F dopants affects the overall reaction efficiency. As shown in Fig. 6D, the apparent quantum efficiency (AQE) of MB degradation at each centered wavelength of the monochromatic light was calculated. The broad action spectrum of the AQE is superimposed with the photoabsorption of the NFT-500 (350 ~ 500 nm) and MB (400 ~ 700 nm). The MB can be excited inevitably in the longer wavelength range over 500 nm due to its intense photoabsorption than NFT-500. However, it was found that the action spectrum below the 460 nm was well agreement with the photoabsorption of NFT-500 instead of negligible feature from the MB. To exclude the possible influence from MB on the evaluation of photocatalytic efficiency, the 420 ~ 440 nm band pass filter was introduced in the

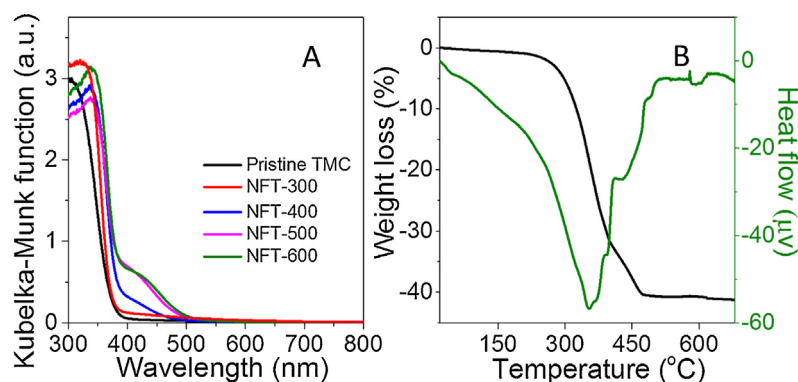


Fig. 5. (A) Steady state diffuse reflectance spectra of NFT with various temperatures (NFT-300 ~ 600) compared with the pristine TMC, and (B) TG-DTA curves of the NH_4TiO_3 in N_2 .

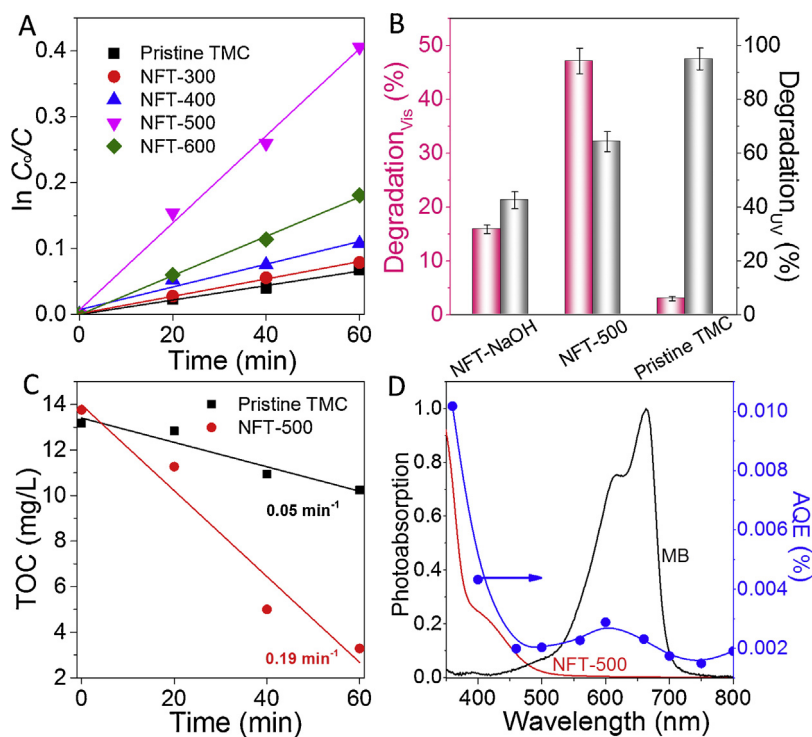


Fig. 6. (A) Photoreduction of Cr(VI) between pristine TMC and NFT under the visible light irradiation. (B) Comparison of MB degradation from pristine TMC, NFT-500, and NFT-NaOH under the visible or UV light irradiation. (C) Kinetics of disappearance of total organic carbon (TOC) by NFT-500 and pristine TMC in photocatalytic degradation of MB under the visible light irradiation. (D) Action spectrum of (right axis, blue line) and photoabsorption (left axis, red line) of the NFT-500 in photocatalytic degradation of MB and visible absorption spectrum of MB (black line). (For interpretation of the references to color in this figure legend, the reader is referred to the web version of this article.)

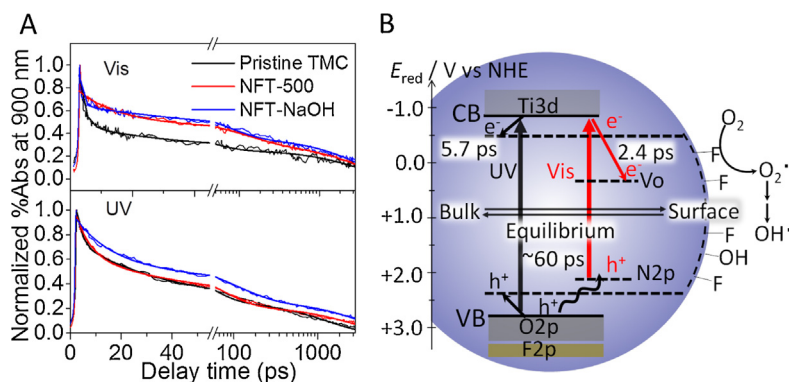


Fig. 7. (A) Normalized transient absorption trace from pristine TMC, NFT-500, and NFT-NaOH under the visible or UV laser irradiation. (B) Schematic illustration of the spatial and energetic distribution of electrons and holes in NFT after excitation at 440 nm (red arrow) and 330 nm (black arrow). The V_o denotes the oxygen vacancy. (For interpretation of the references to color in this figure legend, the reader is referred to the web version of this article.)

Table 2

Kinetic parameters of decays for pristine TMC, NFT-500, and NFT-NaOH under the visible or UV light excitation.

Sample	Visible light			UV light		
	τ_1 [ps]	τ_2 [ps]	τ_3 [ps]	τ_1 [ps]	τ_2 [ps]	τ_3 [ps]
Pristine TMC	1.1 (48%)	27 (26%)	2945 (26%)	2.1 (52%)	36 (32%)	1288 (16%)
NFT-500	2.1 (33%)	52 (33%)	2751 (34%)	5.2 (46%)	60 (33%)	2510 (21%)
NFT-NaOH	0.5 (34%)	63 (30%)	3086 (36%)	13.2 (40%)	110 (33%)	3298 (27%)

experiments. The AQE of the NFT-500 reached 0.004% at 400 nm and 0.002% at 460 nm to confirm the promising photocatalytic activity in the visible light region. A.

3.3. Charge transfer dynamics and reaction mechanism on doped TMC

As a powerful technique, the femtosecond TDR spectroscopic measurement was performed to clarify the charge carrier dynamics in the photocatalytic reaction under the visible or UV light irradiation (Fig. 7A). The schematic illustration of the energy diagram is shown in Fig. 7B. After the sufficient generation of charge carriers upon the 440-nm laser excitation of NFT-500, electrons are excited from N 2p in the isolated midgap state to the conduction band Ti 3d to be directly trapped (τ_1 , 2.1 ps; Table 2) on the adjacent oxygen vacancy (Vo) generated from the codoping (red line in Fig. 7B) [31,36]. On the other hand, the generated holes are separated and localized at the N 2p state at the same time. After the equilibrium between electrons in the surface trap and the bulk (τ_2 , 52 ps; Table 2), the favorable reduction pathway and charge recombination occur (τ_3 , 2751 ps; Table 2) in NFT-500. Generally, a longer lifetime of charge carrier enhances the photocatalytic efficiency. However, it is unusual that NFT-NaOH with the lower efficiency exhibited longer lifetimes of two components (τ_2 , 63 ps; τ_3 , 3086 ps) than those for NFT-500, showing the similar photocatalytic efficiency under the UV irradiation (see below). The shorter lifetime of NFT-NaOH (τ_1 , 0.5 ps) observed at the first decay component corresponds to the inequivalent oxygen atom at the deep state of Vo because F is removed in NFT-NaOH as compared in NFT-500 [31,32]. The time profile of the transient adsorption at 900 nm for pristine TMC is not discussed here, because it is probably resulted from unknown impurities. Under the UV laser excitation at 330 nm, the generated electrons and holes on pristine TMC are usually trapped at the surface defects (τ_1) separately to yield reductive oxygen species (black line) with enhancing photocatalytic efficiency (longer τ_2 and τ_3) [30]. In this case, NFT-500 showed three components 5.2 ps (τ_1), 60 ps (τ_2), and 2510 ps (τ_3) in Fig. 7A and Table 2. Compared with those for pristine TMC, 2.1 ps (τ_1), 36 ps (τ_2), and 1288 ps (τ_3) in Table 2, it is shown that the slower recombination process on NFT-500 corresponds to the hole localized on the N 2p state in Fig. 7B [37,38]. On the other hand, the efficient charge separation of NFT-500 was observed with the lower photocatalytic efficiency under the UV irradiation compared to that for pristine TMC, suggesting the low yield of hydroxyl radical because of less positive potential of N in the localized midgap state (Fig. 7B) [39]. Compared with NFT-500 under the same irradiation condition, NFT-NaOH showed low photocatalytic efficiency even though the longer lifetime, 13.2 ps (τ_1), 110 ps (τ_2), and 3298 ps (τ_3). It has been reported that the surface adsorbed F[−] replaces the sites of adsorbed OH[−] ($\equiv\text{Ti}-\text{OH}+\text{F}^- \rightarrow \equiv\text{Ti}-\text{F}+\text{OH}^-$) for NF-doped TiO₂ [31,32], suggesting the electron flow occurs to O₂ through $\equiv\text{Ti}-\text{F}$ to yield superoxide anion (O₂^{•−}) which changes to hydroxyl radical (OH[•]) via the protonation and O–O bond cleavage processes [30]. Therefore, the higher amount of OH[•] is accomplished together with the preferential adsorption of MB (cationic dye) on the surface for NFT-500 (Fig. S9) to show the higher photocatalytic efficiency under the visible light irradiation [30,32].

4. Conclusions

In this present work, we were successfully synthesized NFT with N and F codopants into TMC during the topochemical transformation. The NFT with (001) facet exposed exhibited uniform distribution of two dopants depending on the annealing temperature. Their reductive photocatalytic efficiency from Cr(VI) to Cr(III) was consistent with the optical absorption by N in the isolated midgap state, which is doped with a certain amount after the annealing. It is found that NFT-500 exhibited the highest photocatalytic efficiency due to the highest concentration of N with the surface modification from F coupling. Together with the charge transfer dynamics, the poor degradation of MB for NFT-NaOH under the visible or UV light irradiation is explained by the effect of F codoping with high yield hydroxyl radical and preferential adsorption, accompanying with assistant role to N in the localized midgap state. TMC with N and F codoping presents a particular interest on promising visible light driven photocatalytic efficiency and allows us to devote the effect on developing new materials as the photocatalyst.

Acknowledgements

The authors thank Dr. M. Kuroda and Prof. M. Ike, Osaka University, for TOC measurement. This work has been partly supported by Innovative Project for Advanced Instruments, Renovation Center of Instruments for Science Education and Technology, Osaka University, and a Grant-in-Aid for Scientific Research (Project 25220806, 25288035, and others) from the Ministry of Education, Culture, Sports, Science and Technology (MEXT) of the Japanese Government. We are thankful for the help of the Comprehensive Analysis Center of SANKEN, Osaka University.

Appendix A. Supplementary data

Supplementary data associated with this article can be found, in the online version, at <http://dx.doi.org/10.1016/j.apcatb.2015.12.022>.

References

- [1] A. Fujishima, K. Honda, *Nature* 238 (1972) 37–38.
- [2] Y. Ma, X. Wang, Y. Jia, X. Chen, H. Han, C. Li, *Chem. Rev.* 114 (2014) 9987–10043.
- [3] L. Wang, T. Sasaki, *Chem. Rev.* 114 (2014) 9455–9486.
- [4] Y. Bai, I. Mora-Sero, F. De Angelis, J. Bisquert, P. Wang, *Chem. Rev.* 114 (2014) 10095–10130.
- [5] M.G. Walter, E.L. Warren, J.R. McKone, S.W. Boettcher, Q. Mi, E.A. Santori, N.S. Lewis, *Chem. Rev.* 110 (2010) 6446–6473.
- [6] J. Schneider, M. Matsuoka, M. Takeuchi, J. Zhang, Y. Horiuchi, M. Anpo, D.W. Bahnemann, *Chem. Rev.* 114 (2014) 9919–9986.
- [7] L. Sang, Y. Zhao, C. Burda, *Chem. Rev.* 114 (2014) 9283–9318.
- [8] M. Pelaez, N.T. Nolan, S.C. Pillai, M.K. Seery, P. Falaras, A.G. Kontos, P.S.M. Dunlop, J.W.J. Hamilton, J.A. Byrne, K. O'Shea, M.H. Entezari, D.D. Dionysiou, *Appl. Catal. B: Environ.* 125 (2012) 331–349.
- [9] R. Asahi, T. Morikawa, H. Irie, T. Ohwaki, *Chem. Rev.* 114 (2014) 9824–9852.
- [10] W.J. Ong, L.L. Tan, S.P. Chai, S.T. Yong, A.R. Mohamed, *Nanoscale* 6 (2014) 1946–2008.
- [11] D. Chen, Z. Jiang, J. Geng, J. Zhu, D. Yang, *J. Nanopart. Res.* 11 (2008) 303–313.
- [12] M. Hojamberdiev, G. Zhu, P. Sujaridworakun, S. Jinawath, P. Liu, J.P. Zhou, *Powder Technol.* 218 (2012) 140–148.

- [13] Y. Liu, Y. Zhang, H. Tan, J. Wang, *Cryst. Growth Des.* 11 (2011) 2905–2912.
- [14] Y. Liu, Y. Zhang, H. Li, J. Wang, *Cryst. Growth Des.* 12 (2012) 2625–2633.
- [15] Y. Liu, Y. Zhang, J. Wang, *CrystEngComm* 15 (2013) 791–801.
- [16] H.K. Lee, S.W. Lee, *Chem. Lett.* 44 (2015) 604–606.
- [17] T. Tachikawa, T. Majima, *NPG Asia Mater.* 6 (2014) e100.
- [18] G. Liu, H.G. Yang, J. Pan, Y.Q. Yang, G.Q. Lu, H.M. Cheng, *Chem. Rev.* 114 (2014) 9559–9612.
- [19] L. Bergström, E.V. Sturm, G. Salazar-Alvarez, H. Cölfen, *Acc. Chem. Res.* 48 (2015) 1391–1402.
- [20] Y. Liu, Y. Zhang, J. Wang, *CrystEngComm* 16 (2014) 5948–5967.
- [21] C. Di Valentin, E. Finazzi, G. Pacchioni, A. Selloni, S. Livraghi, A.M. Czoska, M.C. Paganini, E. Giamello, *Chem. Mater.* 20 (2008) 3706–3714.
- [22] Z. Bian, T. Tachikawa, T. Majima, *J. Phys. Chem. Lett.* 3 (2012) 1422–1427.
- [23] P. Zhang, T. Tachikawa, Z. Bian, T. Majima, *Appl. Catal. B: Environ* 176–177 (2015) 678–686.
- [24] Bian, T. Tachikawa, P. Zhang, M. Fujitsuka, T. Majima, *Nat. Commun.* 5 (2014) 3038.
- [25] L. Zhou, D. Smyth-Boyle, P. O'Brien, *J. Am. Chem. Soc.* 130 (2008) 1309–1320.
- [26] T.R. Gordon, M. Cargnello, T. Paik, F. Mangolini, R.T. Weber, P. Fornasiero, C.B. Murray, *J. Am. Chem. Soc.* 134 (2012) 6751–6761.
- [27] W. Wang, C. Lu, Y. Ni, M. Su, W. Huang, Z. Xu, *Appl. Surf. Sci.* 258 (2012) 8696–8703.
- [28] W. Wang, Y. Ni, C. Lu, Z. Xu, *Appl. Surf. Sci.* 290 (2014) 125–130.
- [29] J. Wang, D.N. Tafen, J.P. Lewis, Z. Hong, A. Manivannan, M. Zhi, M. Li, N. Wu, *J. Am. Chem. Soc.* 131 (2009) 12290–12297.
- [30] J.I. Brauer, G. Szulcowski, *J. Phys. Chem. B* 118 (2014) 14188–14195.
- [31] N. Kumar, U. Maitra, V.I. Hegde, U.V. Waghmare, A. Sundaresan, C.N. Rao, *Inorg. Chem.* 52 (2013) 10512–10519.
- [32] J. Cheng, J. Chen, W. Lin, Y. Liu, Y. Kong, *Appl. Surf. Sci.* 332 (2015) 573–580.
- [33] S. Gurdip, P. Inder, K. Jaspreet, *Indian J. Eng. Mater. Sci.* 7 (2007) 229–235.
- [34] W. Kim, T. Tachikawa, H. Kim, N. Lakshminarasimhan, P. Murugan, H. Park, T. Majima, W. Choi, *Appl. Catal. B: Environ.* 147 (2014) 642–650.
- [35] P. Zhang, T. Tachikawa, M. Fujitsuka, T. Majima, *Chem. Commun.* 51 (2015) 7187–7190.
- [36] K. i. Yamanaka, T. Morikawa, *J. Phys. Chem. C* 116 (2012) 1286–1292.
- [37] H.C. Wu, Y.S. Lin, S.W. Lin, *Int. J. Photoenergy* 2013 (2013) 1–7.
- [38] J.B. Varley, A. Janotti, C.G. Van de Walle, *Adv. Mater.* 23 (2011) 2343–2347.
- [39] J.W.J. Hamilton, J.A. Byrne, P.S.M. Dunlop, D.D. Dionysiou, M. Pelaez, K. O'shea, D. Synnott, S.C. Pillai, *J. Phys. Chem. C* 118 (2014) 12206–12215.